Quasi-two-dimensional properties of a single shallow-water vortex with high initial Reynolds numbers

D.-G. SEOL† AND G. H. JIRKA‡

Institute for Hydromechanics, Karlsruhe Institute of Technology, Kaiserstr. 12,
Karlsruhe 76131, Germany

The evolution and dynamics of a shallow-water vortex system with high initial Reynolds numbers are investigated experimentally without background rotation. A single vortex is generated by rotating a water mass at the centre of an experimental tank using a bottomless cylinder with internal sectors. The surface velocity field is observed via particle image velocimetry. The experimentally observed vorticity fields indicate that strong shallowness (the ratio of the cylinder diameter to the water depth) and high Reynolds number contribute to the formation of large-scale coherent structures in the form of a tripolar vortex system. The shallow-water vortices with high initial Reynolds numbers experience the transition from turbulent to laminar regimes in their decay process. The proposed first-order vortex decay model predicts that a shallow-water vortex decays as t^{-1} in the initial turbulent stage and as e^{-t} in the later laminar stage due to horizontal diffusion and bottom friction. The estimated transition time scale from the turbulent to laminar stage increases with initial vortex Reynolds number and with shallowness. By taking the vortex expansion into consideration, the second-order vortex decay model is also presented. The azimuthally ensemble-averaged data elucidate effects of the vortex instabilities and of turbulent energy transfer on the formation of large-scale coherent flow structures. Normal mode analysis of the vortex systems is conducted to study the effect of shallowness and Reynolds number on the generation of two-dimensional large-scale coherent structures. The results show that the perturbation wavenumber of mode 2 is the fastest-growing instability in shallow-water conditions, and its effect depends on initial Reynolds number and shallowness.

Key words: shear layer turbulence, vortex dynamics, vortex instability

1. Introduction

Coherent large-scale vortices in shallow-water conditions can be found in many natural and engineering applications. Topographical forcing (e.g. islands, headlands, groynes, etc.) creates velocity variations in the transverse direction and causes initial flow instabilities (Jirka & Uijttewaal 2004). Because of the confinement provided by flow depth, these instabilities grow in the horizontal dimension and lead to the

† Present address: Chonnam National University, Yosu 550-749, South Korea. Email address for correspondence: seol@ifh.uka.de
‡ Deceased on 14 February 2010

generation of large-scale predominantly two-dimensional coherent structures (2DCS), whose horizontal length scale is much larger than the water depth (Uijttewaal & Booij 2000). These flow structures are important for controlling the mass, momentum and heat transport of the flow, and thereby strongly influence the mixing processes of pollutants and the erosion process at the bottom surface (Lin, Ozgoren & Rockwell 2003; Carmer, Rummel & Jirka 2004). The main signatures of these inherently turbulent shallow flows are the inverse energy cascade leading to quasi-two-dimensional large-scale coherent flow structures (Jirka 2001). The study of an isolated single vortex in shallow flows can provide a basis for understanding the more complex turbulent flows.

The limits on the 'geometrical confinement' for quasi-two-dimensional flow have not yet been determined clearly. As a previous study to answer this question, Paret *et al.* (1997) generated monopolar and dipolar structures electromagnetically to investigate the physical process suppressing the three-dimensional effect by shallowness (e.g. 6 mm thick two-layered NaCl solution in 20 cm × 27 cm PVC cell in their study). They found that the flow could be treated as two-dimensional flow after a short transition time. Sous, Bonneton & Sommeria (2005) also concluded that the damping of the vertical motion by the water depth is responsible for the formation of large-scale horizontal flow structures, such as a vortex dipole. Later, the effect of vertical restriction on the flow was numerically confirmed for an evolving axisymmetric monopolar vortex in shallow fluid by Satijn *et al.* (2001). They also found that the two-dimensionality depends not only on the geometrical confinement but also on the Reynolds number. This is due to the secondary flow generated by the no-slip bottom boundary. From the previous studies, it was concluded that the vertical velocity structures in quasi-two-dimensional flow relaxes to a Poiseuille flow, which is usually modelled by a Rayleigh bottom friction term (Clercx, van Heijst & Zoeteweij 2003; Akkermans *et al.* 2008). This bottom friction effect also has an influence on the peak vorticity resulting in rapid attenuation of the vorticity level for the conditions of shallow-water depth (Lin *et al.* 2003).

In this experimental study, we restrict our flow conditions to the shallow single-vortex flow over limited length scales below the Rossby radius (in fact, without any Coriolis force) and to initial conditions with high Reynolds numbers. Therefore, in the absence of Coriolis effects (i.e. large Ekman number), the evolution of the flow field is primarily governed by the interplay of inertial and viscous effects, the latter linked to horizontal as well as to bottom shear stresses. By setting these limits, we emphasize the purpose of our study towards small-scale geographical applications, such as shallow vortices behind small islands (e.g. Chen & Jirka 1995), or tidal efflux eddies from coastal lagoons (e.g. Chen & Jirka 1995; Wells & van Heijst 2003; Nicolau del Roure, Socolofsky & Chang 2009), or engineering applications such as vortex shedding behind groynes in rivers (e.g. Sukhodolov, Uijttewaal & Engelhardt 2002). The Reynolds numbers in our experiment of $O(10^4 \sim 10^5)$, based on initial peripheral velocities and water depth, are large enough to exhibit a Reynolds-invariant turbulent regime, similar to the field situation, and the ratio of horizontal vortex length scale to water depth $O(10)$ is also similar.

In two-dimensional confined flow conditions, the turbulent flow undergoes reorganization to form a coherent multipole vortex system. Monopolar vortices may emerge in two-dimensional turbulence from an initial state of randomly distributed vorticity fields (McWilliams 1984). Dipoles can be formed when two of such vortices with oppositely signed circulations interact to create a self-propelling compound vortex. The emergence of tripolar vortices was first observed by Legras, Santangelo &

Benzi (1988) in numerical simulations of randomly distributed vortices. Carton, Flierl & Polvani (1989) numerically studied the generation of tripoles from an unstable axisymmetric isolated monopolar vortex. The formation of a stable tripolar vortex from an unstable axisymmetric vortex was investigated experimentally in a rotating homogeneous fluid (van Heijst & Flór 1989; van Heijst & Kloosterziel 1991). It was found that the tripole formation is the result of an azimuthal wavenumber 2 instability of an unstable isolated circular vortex. This tripole vortex has been observed, for example, in the Bay of Biscay as a result of topographic destabilization of oceanic eddies (Pingree & Le Cann 1992; Carton 2001). From further laboratory and numerical experiments, triangular and square vortices due to the wavenumber 3 and 4 instabilities were also reported (Carnevale & Kloosterziel 1994; Beckers & van Heijst 1998; Kloosterziel & Carnevale 1999). One of the main purposes of the present study is to investigate the correlation between the flow instabilities and the flow conditions.

We investigate experimentally a single large-scale vortex as a precursor to future studies of a more complex multiple vortex system. Different methods to create a single vortex have been used in laboratory experiments. A comprehensive review on the laboratory techniques for single-vortex generation in a rotating fluid can be found in van Heijst & Clercx (2009). To generate an isolated vortex (the net vorticity is zero), Kloosterziel & van Heijst (1991) stirred the water mass inside a hollow cylinder in a rotating tank. After the flow inside the cylinder is stabilized to purely azimuthal, they released the single vortex by removing the cylinder wall. A similar technique has been used to generate a self-propagating quasi-monopolar vortex with angular momentum and linear momentum (Voropayev et al. 1999). Another generation technique is the sink technique, in which the cyclonic vortex is produced by pumping out some fluid through a sink (e.g. a perforated tube). For this method, a background rotation is necessary for fluid parcels to be deflected to one side while moving towards a sink. The vortex generated by this method is non-isolated (Kloosterziel & van Heijst 1992; Zavala Sansón & van Heijst 2002). A third method is the gravitational collapse technique (Kloosterziel & van Heijst 1992). A thin-walled open cylinder is placed in the rotating fluid tank, and the fluid level inside this cylinder is lower than that of the outside. When the cylinder is lifted, a gravity-driven flow arises in the radial direction immediately followed by a deflection due to the Coriolis acceleration. This method is dynamically similar to the stirring method. A baroclinically forced cyclonic vortex can also be generated by placing an ice cube inside a circular hollow cylinder in the rotating water tank (Cenedese, Adduce & Fratantoni 2005). These previous vortex generation methods require background rotation to achieve two-dimensionality of the vortex, where the background rotation suppresses any variation of the flow in the vertical direction (Orlandi & Carnevale 1999). In stratified fluids, a single vortex was created by a rotating sphere, a thin bent rod, or injecting fluid along the inner wall of a submerged open cylinder (Flór & van Heijst 1996; Trieling & van Heijst 1998). These studies shed light on the importance of vertical as well as horizontal diffusion in vortex decay. Furthermore, vortex flow can be initiated by electromagnetic forcing in an electrolyte fluid (e.g. mercury, salt solution) (Nguyen Duc & Sommeria 1988; Akkermans et al. 2008), although this method generally generates vortex couples due to the inherent properties of the magnetic force fields.

In our experiments, a single vortex is generated by the initial solid body rotation of a fluid mass within a rotating open-bottom cylinder that is lifted out of the water at the start of the experiment. The subsequent instabilities, turbulent growth and decay of the resulting vortex are the objectives of the study.
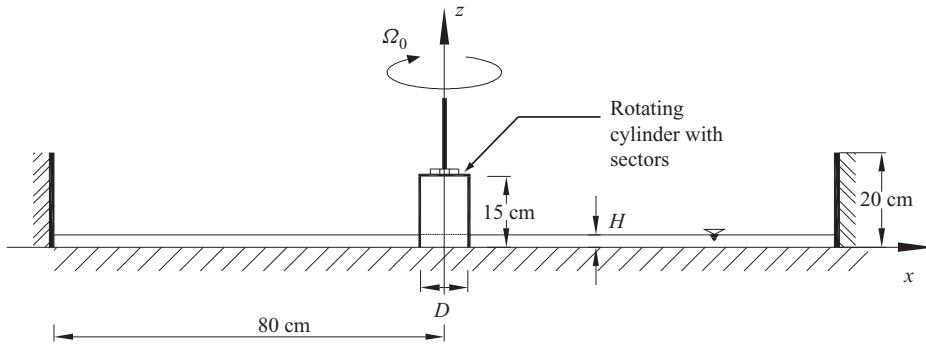
FIGURE 1. Experimental set-up.

The paper is organized as follows. In §2, we describe the experimental procedures and analysis methods. In §3, we present the general properties of a single vortex with different Reynolds numbers and shallowness conditions. In §4, we discuss the global vortex decay properties. The physical properties of the ensemble averaged shallow vortex are presented in §5. Final conclusions are given in §6.

2. Experiments

2.1. *Generation of single vortex*

The laboratory experiments were conducted in a shallow-water tank with a dimension of $160 \, \text{cm} \times 160 \, \text{cm} \times 20 \, \text{cm}$ without background rotation. The size of the tank is large enough to prevent any disturbances from the sidewalls. For optical access, the tank bottom and sidewalls are made with glass and Plexiglas, respectively. The experimental tank was filled with regular tap water at room temperature with different depths to test shallowness effects. The vortex generator consists of a bottomless Plexiglas cylinder, divided into several sectors, mounted vertically and driven by a stepper motor, and is mounted on a movable bridge. The generation system is controlled by a PC. A schematic side view of the experimental set-up is shown in figure 1.

Prior to the experiment, the tank is filled with a water depth of H. For vortex generation, the water mass inside the cylinder is rotated during an initial spin-up time (4 s). This spin-up from the situation at rest causes four principal disturbances. (i) The surface-water level is disturbed with a deflection, $\Delta h = \Omega_0^2(r^2 - R_0^2/2)/2g$, in which Ω_0 is the initial angular velocity, r is the radius from centre, R_0 is the cylinder radius and g is the gravitational acceleration. Upon removal of the cylinder, this causes surface waves in the tank. In order to minimize the waves, the maximum deflection, $\Delta h(R_0) = \Omega_0^2 R_0^2/4g$, is kept small (less than 1 cm). (ii) Internal circulations are set up within the internal sectors installed within the cylinder. Given that sufficient internal sectors are installed (typically 4–8 sectors), these circulations are sufficiently weak as observed by a camera and diminish rapidly compared to the time subjected to initial forcing in which the flow becomes the solid body rotation. (iii) The excess of pressure at the cylinder periphery causes some leakage losses through the gap between the rotating cylinder wall and the tank bottom (less than 0.5 mm). A sufficiently small gap and the short spin-up time (4 s) were found adequate to minimize the losses. (iv) As the cylinder is removed from the water, we observe strong turbulent mixing followed by water inflow and surface waves in the radial direction due to the displaced cylinder wall volume. This radial inflow is overwhelmed by the rotational flow in a

Experiment number	Water depth H (cm)	Initial angular velocity Ω_0 (1/s)	Cylinder diameter D (cm)	Number of internal sectors	Shallowness $S = D/H$ (−)	Reynolds number Re (−)
I	2	3.14	10	4	5	7850
II	2	6.28	10	4	5	14 000
III	2	9.42	10	4	5	21 000
IV	2	12.56	10	4	5	28 000
V	3	6.28	10	4	3.3	14 000
VI	4	6.28	10	4	2.5	14 000
VII	5	6.28	10	4	2	14 000
VIII	6	6.28	10	4	1.7	14 000
IX	2	6.28	20	8	10	56 000

TABLE 1. Experimental conditions.

few rotations. The generated surface waves are damped out and have little influence on the vortex formation as observed by van Heijst & Kloosterziel (1991).

Table 1 summarizes the experimental programme, in which the effects of initial angular velocity Ω_0, water depth H and cylinder diameter D have been studied. The shallowness and the Reynolds number for the study are defined by $S = D/H$ and $Re = V_0 R_0 / \nu$ respectively, where V_0 is the initial azimuthal velocity at the cylinder periphery, and ν is the kinematic viscosity of water ($=1.12 \times 10^{-2}$ cm^2 s^{-1}), range from 1.7 to 10 and from 7850 to 56 000, respectively. After a short spin-up time (t_s) of 4 s, the vortex generator is rapidly lifted with the PC-controlled pneumatic cylinder, and the whole vortex generation system is moved outside the tank manually. The time origin ($t = 0$) is defined as the moment when the controlling PC sends a signal to remove the vortex-generating cylinder from the water. Note that the cylinder is still rotating while it is lifted up from the water.

2.2. *Measurements on surface flow fields*

To obtain quantitative information about the flow field, surface particle image velocimetry (PIV) was applied. In this study, we consider the surface velocity field as being representative of the underlying flow field. It is noteworthy, however, that an adequate ratio between average cross-sectional and surface velocities is proposed as 0.85–0.90 by assuming a logarithmic velocity profile (Creutin *et al.* 2003). This means that the measured surface flow field overestimates the mean flow properties by around 10 %. Furthermore, we also assume that the secondary flow due to the secondary circulation near the bottom has negligible effects on the vortex instability. As reported in Sous *et al.* (2005), the ratio of the kinetic energy associated with the vertical and horizontal velocity components decreases below 0.10 for strong shallowness ($C \geqslant 3$, where C represents the vertical confinement coefficient by Sous *et al.* 2005; this can be converted to $S \approx 5$ in this study).

The experimental set-up for surface PIV is rather simpler than the conventional laser PIV system. The flow field is illuminated with normal floodlights and seeded with buoyant polyester glitter particles with size distribution of 0.5–1.5 mm (Sigmund Lindner GmbH). The images of the tracer particles are recorded using a CCD camera (Imager Compact, LaVision GmbH, 1024 pixel × 1024 pixel with 12-bit greyscale intensity) with a Nikkor 15 mm wide-angle lens. The camera is mounted at 285 cm directly above the water surface to cover a measurement area of about 130 cm × 130 cm (maximum 2.5 % of image distortion at the image edge). The tracer particle images

are taken in a single-frame mode with a frequency of 10 Hz with the exposure time of 50 ms. The measurements are taken for 2 min, which is long enough to record the whole lifetime of the vortex system. To account for the initial disturbances (e.g. removing the vortex generator, dripping waters from the cylinder, etc.) in the flow fields, the measurements for the first 2 s are not considered for the analysis of the flow fields.

A commercial PIV software (DaVis 6.2, LaVision GmbH) is used to process the captured images to obtain a velocity vector field. Contrary to a typical PIV image of individual tracer particles, the recorded image in the surface PIV appears as a brightness pattern image of groups of moving particles in the flow (Fujita, Muste & Kruger 1998). In this type of image, the measurement error was estimated about 5 % with the seeding density (the percentage ratio of seeded to total image area) of 33 % (Meselhe, Peeva & Muste 2004). The adaptive-multipass algorithm is used for the PIV processing with decreasingly smaller interrogation window size based on cross-correlation. The initial and final interrogation window sizes were 128 pixel × 128 pixel and 32 pixel × 32 pixel with 50 % overlapping region, respectively. The resulting data resolution is about 2 cm. To remove erroneous velocity vectors, the vector maps have been post-processed using a velocity median filter.

From the obtained velocity vector field, the vertical component of vorticity, ω, is determined as

$$\omega = \frac{\partial v}{\partial x} - \frac{\partial u}{\partial y}, \tag{2.1}$$

where u and v are the horizontal velocity components at the water surface. The vorticity field was estimated using the least-squares approach by calculating spatial derivatives of the local velocity gradient (Raffel, Willert & Kompenhans 1998).

2.3. *Coordinate transformation*

We assume that the initial shallow vortex flow field is purely azimuthal, where the fluid rotates about the axis. In the study of the axisymmetric rotating flow structures, it is convenient to transform from a Cartesian to a polar coordinate system. Both the vorticity maximum and the streamfunction maximum can be used to determine the vortex centre for the coordinate system transformation. The method based on the maximum vorticity did not work very well for the case where the centre vortex has a hollow vorticity region, such as in the early stage just after the cylinder is removed from the water. In addition, the maximum streamfunction method also failed due to inaccuracies introduced in integrating the velocity field to obtain the streamfunction. Therefore, we define the vortex centre in the following manner. First, the vorticity field is separated by its sign, in which the central vortex has a positive sign (clockwise rotation). Second, the vorticity contours satisfying $\omega = \delta\,\omega_{max}$, where δ is a constant varying 0.5–0.7 and ω_{max} is the measured maximum vorticity, are defined from the separated vorticity field. Finally, the vortex centre is defined by calculating the centre of a mass within the contour area. With the defined vortex centre, the azimuthal and radial components of velocity, v_θ and v_r, can be calculated from the Cartesian velocities u and v in x and y direction for the radial distance, r, and the azimuthal angle, θ.

2.4. *Azimuthal average*

Each experimental condition is repeated about 7–10 times and ensemble-averaged to ensure repeatability and to gain insight on the mean flow properties of the generated shallow vortex system. For azimuthal averaging, each instantaneous flow field is converted to a polar coordinate system as explained in §2.3. It is difficult to superimpose all the vortices for the average in a Cartesian coordinate system due to
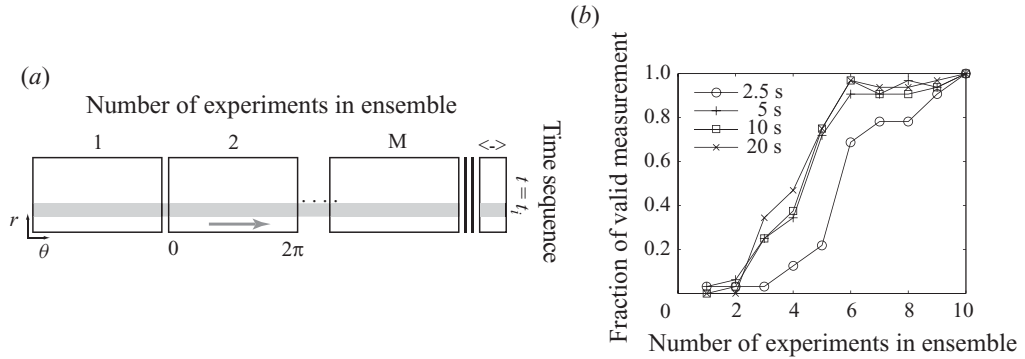
FIGURE 2. Ensemble-averaging of vortex system in azimuthal direction: (*a*) schematic of the process and (*b*) estimated fraction of valid measurements for the number of experiments in ensemble.

the random distribution of small vortex patches around the central vortex at an early stage. After conversion to a polar coordinate system, the velocity components (v_r and v_θ) are averaged over the azimuthal direction. As shown in figure 2(*a*), the azimuthal averages of the velocity components are ensemble-averaged over the total number M of instantaneous velocity fields.

The performance of the ensemble-averaging can be quantified by calculating the fraction of valid measurements for the number of experiments in the ensemble (Meinhart, Wereley & Santiago 2000). To quantify the convergence of the ensemble average, the fraction of valid measurements was estimated by counting the number of azimuthal velocity components that are deviated by more than 10 % from the ensemble-averaged velocity profile with 10 data sets. Figure 2(*b*) shows the estimated fraction of valid measurements as a function of the number of experiments used in the ensemble average. As shown in the figure, about 95 % convergence can be achieved by ensemble-averaging more than five data sets, except for the very first stage (e.g. 2.5 s), where the flow is still in a highly unstable turbulent condition. This test proves the convergence of the ensemble average provided more than five data sets are used.

3. General observations

3.1. *Initial development of instability*

Instabilities occurring in the initial vortex forcing stage are studied by measuring the flow fields before removing the cylinder (figure 3). The measurements were conducted by installing the camera below the experimental tank for the experiment II condition. The flow field inside the internal section was not measured due to the optical disturbance by the inner walls. Figures 3(*a*) and 3(*b*) illustrate the velocity and vorticity fields at 2 and 4 s after starting the cylinder rotation, respectively. The flow fields clearly show that the vortex core is surrounded by a ring of opposite-signed vorticity due to the boundary layer outside the rotating cylinder; also, the thickness of the boundary layer grows over time. During the forcing, the flow in this outer boundary layer is already susceptible to centrifugal instability, which is demonstrated well as negative vorticity patches in figure 3(*b*).

3.2. *Effects of Reynolds number*

For different initial angular velocities with the same shallowness ($S = 5$) and a fixed cylinder diameter ($D = 10$ cm) and water depth ($H = 2$ cm), the instantaneous vorticity
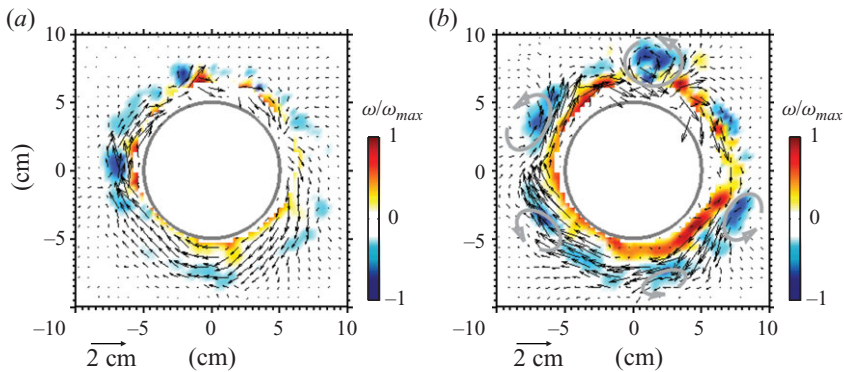
FIGURE 3. Measured velocity and vorticity fields during vortex forcing stage for experiment II: 2 s (*a*) and 4 s (*b*) after starting cylinder rotation. Vorticity countours are normalized with observed maximum vorticity value.

maps at different times were plotted in figure 4. For all conditions, positive vorticity (shown in red) has been created inside the cylinder (grey circle represents the initial position of the cylinder). It can be observed that patches of negative vorticity (shown in blue) are created and slowly rotate around the central vortex in the anti-clockwise direction. For higher initial angular velocities, the central vortex has a more irregular shape. While rotating, the outside vortex patches reorganize themselves (mainly merging with neighbouring vorticity patches) and form two large patches of negative-signed vorticity (satellite vortices). It appears that all cases converge to form a tripole system, even though the low-Reynolds-number case does not fully complete the tripole formation process (see figure 4*d*). In all these shallow cases, the horizontal scale of the final vortices greatly exceeds the water depth H (indicated by the error bar of 2 cm length in figures 4*a*, 4*e*, 4*i* and 4*m*). This observed sequence is dominated by the following mechanics: the initial solid body rotating mass after removal of the cylinder forms a single vortex surrounded by a ring of opposite-signed vorticity in the outer boundary layer. The action of these opposite vorticity patches develops azimuthal instabilities. According to the two-dimensional vortex linear stability analysis (Flierl 1988), an azimuthal wavenumber k instability may deform the annulus into k satellite vortices surrounding the core vortex based on the relative width of the outer annulus of the opposite-signed vorticity. After the cylinder removal, vigorous vertical and horizontal mixing occur around the central vortex. This turbulent mixing triggers the instabilities around the central vortex. Except for the low-Reynolds-number case, where the azimuthal wavenumber 4 instability is dominating (figures 4*a*, 4*b*, 4*c*), the competition between unstable modes of different wavenumbers can be observed in the early stage of the vorticity maps (Carnevale & Kloosterziel 1994). As shown in the plots for low initial rotational velocity, the negative vorticity patches are nearly stagnant at the beginning and slowly merge together to form a tripole. In contrast, for higher initial rotation velocity cases, the azimuthal wavenumber 2 instability is developed and transformed into the tripole system at a much quicker pace than for smaller initial rotation velocity. In summary, it appears that the higher-Reynolds-number cases clearly exhibit a Reynolds-invariant behaviour in that the large-scale flow features at larger times become self-similar. This seems to hold for $Re \geqslant 14\,000$ within the times shown in figure 4.
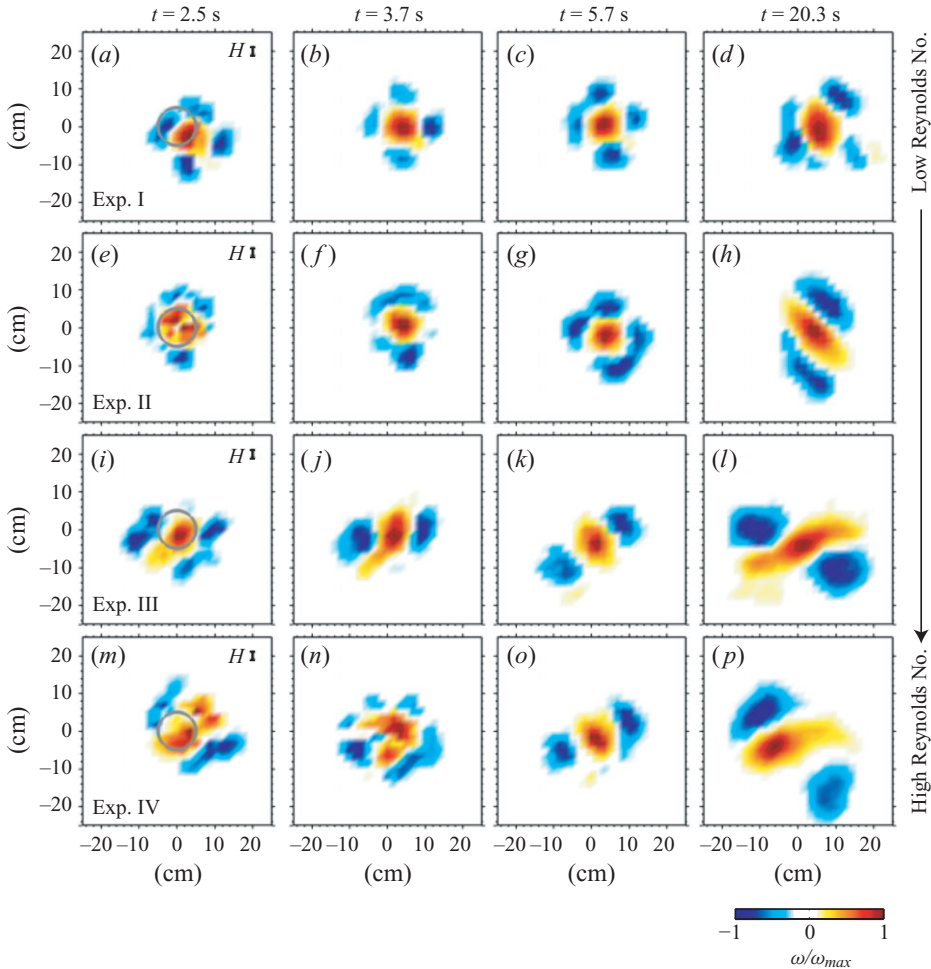
FIGURE 4. Snapshots of instantaneous vorticity maps for different Reynolds numbers with the same shallowness ($S = 5$). (a–d) $Re = 7850$ at $t = 2.5$, 3.7, 5.7 and 20.3 s, respectively, (e–h) $Re = 14\,000$, (i–l) $Re = 21\,000$, (m–p) $Re = 28\,000$. The grey circles and error bars in (a), (e), (i) and (m) represent the initial cylinder contour and water depth, respectively. The vorticity contour levels are normalized with the maximum vorticity value observed in each plot.

3.3. *Effects of shallowness*

Figure 5 shows the time sequence of instantaneous vorticity maps for different shallowness S (2–10) and for high-Reynolds-number cases ($Re \geqslant 14\,000$). This should be compared to figure 4, which corresponds to the case of $S = 5$. It is obvious that the shallowness has a pronounced influence on the distribution of vorticity. Again, error bars in figures 5(a), 5(e), 5(i) and 5(m) indicate the variable water depth H. For the strongest shallowness ($S = 10$), the flow has an irregular vortex distribution in the very initial times within $t = 3.7$ s and starts forming the tripole system after 5 s (figure 5c), in which the horizontal vortex size greatly exceeds the water depth H. On the other extreme, the weak shallowness (i.e. deep) cases ($S = 2.5$ and 2) show a distinctly different flow behaviour. The annulus of the negative vorticity originated from the initial shear boundary layer around the central vortex is stagnating and gradually diffuses with time. This horizontal diffusion, evident from the shape of
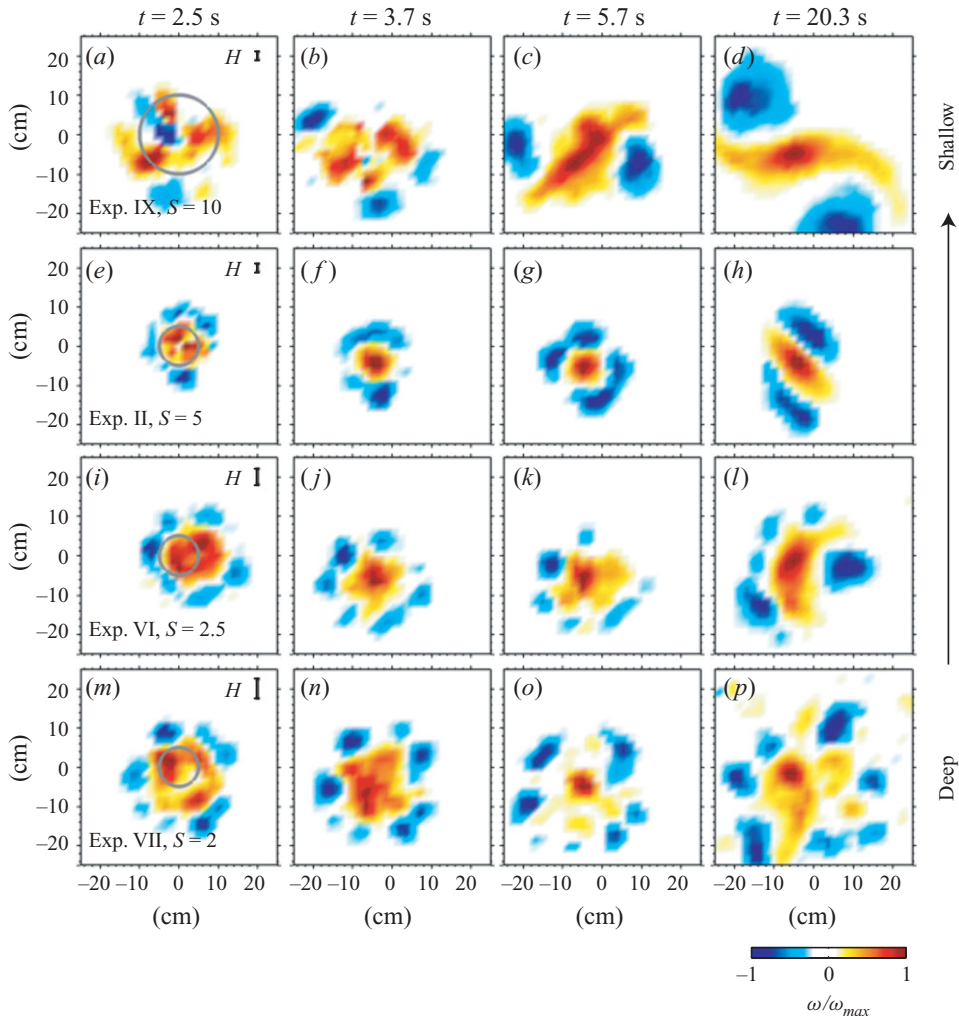
FIGURE 5. Snapshots of instantaneous vorticity maps for different shallowness (S) with the same Reynolds number ($Re = 14\,000$). (a–d) $S = 10$ at $t = 2.5$, 3.7, 5.7 and 20.3 s, respectively, (e–h) $S = 5$, (i–l) $S = 2.5$, (m–p) $S = 2$. The vorticity contour levels are normalized with the maximum vorticity value observed in each plot.

the three-dimensional vortex, whose length scale is below, or at most, of the order of the water depth, leads finally to an irregular turbulent region. This is seen most distinctively in figure 5(p), where the surface signature of the turbulent eddies, mostly in the form of eddies with concentrated negative vorticity at scales of the order of or below the water depth, are visible.

4. Global vortex decay properties

4.1. *Scale analysis on the vortex decay mechanism*

In this section, we attempt to analyse the relative importance of flow scales on the vortex decay as observed in §3. We consider the two-dimensional shallow-water equations for turbulent flow in a fluid layer of depth $h(x, y)$ over a local water bottom

elevation $z_b(x, y)$ obtained by using the hydrostatic approximation

$$\frac{\partial h}{\partial t} + \frac{\partial(h\overline{u})}{\partial x} + \frac{\partial(h\overline{v})}{\partial y} = 0, \tag{4.1}$$

$$\frac{\partial \overline{u}}{\partial t} + \overline{u}\frac{\partial \overline{u}}{\partial x} + \overline{v}\frac{\partial \overline{u}}{\partial y} - f\overline{v} = -g\frac{\partial}{\partial x}(h + z_b) + \frac{v_{eff}}{h}\frac{\partial}{\partial x}\left(h\frac{\partial \overline{u}}{\partial x}\right) + \frac{v_{eff}}{h}\frac{\partial}{\partial y}\left(h\frac{\partial \overline{u}}{\partial y}\right) - \frac{\tau_{bx}}{\rho h}, \tag{4.2}$$

$$\frac{\partial \overline{v}}{\partial t} + \overline{u}\frac{\partial \overline{v}}{\partial x} + \overline{v}\frac{\partial \overline{v}}{\partial y} + f\overline{u} = -g\frac{\partial}{\partial y}(h + z_b) + \frac{v_{eff}}{h}\frac{\partial}{\partial x}\left(h\frac{\partial \overline{v}}{\partial x}\right) + \frac{v_{eff}}{h}\frac{\partial}{\partial y}\left(h\frac{\partial \overline{v}}{\partial y}\right) - \frac{\tau_{by}}{\rho h}, \tag{4.3}$$

in which $\overline{u}$, $\overline{v}$ are the depth-averaged velocities in the horizontal x, y directions, f is the Coriolis parameter, g is the gravitational acceleration, v_{eff} is the effective viscosity as the sum of molecular and turbulent contributions, $v_{eff} = v + v_{turb}$, ρ is the reference fluid density and τ_{bx}, τ_{by} are the turbulent bottom shear stresses in the horizontal x, y directions, expressed by a quadratic friction law,

$$\tau_{bx} = \rho\frac{c_f}{2}\overline{u}\sqrt{\overline{u}^2 + \overline{v}^2}, \qquad \tau_{by} = \rho\frac{c_f}{2}\overline{v}\sqrt{\overline{u}^2 + \overline{v}^2}, \tag{4.4}$$

in which c_f is the bed-friction coefficient (Streeter & Wylie 1985). By taking the curl of the momentum equations and using the continuity equation for constant bottom boundary condition ($z_b = 0$), the conservation equation for the depth-averaged vorticity is given by

$$h\frac{D}{Dt}\left(\frac{\omega + f}{h}\right) = \frac{\partial}{\partial x}\left[\frac{v_{eff}}{h}\frac{\partial}{\partial x}\left(h\frac{\partial \overline{u}}{\partial x}\right) + \frac{v_{eff}}{h}\frac{\partial}{\partial y}\left(h\frac{\partial \overline{u}}{\partial y}\right)\right]$$
$$- \frac{\partial}{\partial y}\left[\frac{v_{eff}}{h}\frac{\partial}{\partial x}\left(h\frac{\partial \overline{u}}{\partial x}\right) + \frac{v_{eff}}{h}\frac{\partial}{\partial y}\left(h\frac{\partial \overline{u}}{\partial y}\right)\right]$$
$$- \frac{\partial}{\partial x}\left(\rho\frac{c_f}{2h}\overline{v}\sqrt{\overline{u}^2 + \overline{v}^2}\right) + \frac{\partial}{\partial y}\left(\rho\frac{c_f}{2h}\overline{u}\sqrt{\overline{u}^2 + \overline{v}^2}\right), \tag{4.5}$$

in which $D(\ )/Dt$ is the material derivative following the fluid motion (Jirka & Seol 2010).

Equation (4.5) expresses the conservation of potential vorticity $(\omega + f)/h$ for a fluid element containing, for example, a 2DCS. In frictionless flow, the potential vorticity is conserved, $D((\omega + f)/h)/Dt = 0$. This is a useful approximation for the inertial behaviour of a vortex flow over short times. In order to evaluate the effect of the turbulence terms in (4.5), we restrict attention to conditions without background rotation, $f \to 0$, and with constant water depth so that (4.5) can be simplified as

$$\frac{D\omega}{Dt} = v_{eff}\left(\frac{\partial^2 \omega}{\partial x^2} + \frac{\partial^2 \omega}{\partial y^2}\right) - \frac{c_f}{2h}\left[\omega\sqrt{\overline{u}^2 + \overline{v}^2} + \overline{u}\frac{\partial}{\partial y}\sqrt{\overline{u}^2 + \overline{v}^2} - \overline{v}\frac{\partial}{\partial x}\sqrt{\overline{u}^2 + \overline{v}^2}\right]. \tag{4.6}$$

A change of vorticity for the 2DCS-like vortex elements is therefore induced by the two terms on the right-hand side of (4.6). The first term describes the turbulent diffusion of vorticity due to the turbulent growth of the vortex element. The second term represents the spin-down of the vortex element due to turbulent bottom friction acting at its base. In principle, both effects can decrease the vorticity in the core region of the vortex element.

A scaling argument shows, however, that in shallow flows the bottom friction effectively controls the vortex spin-down. For that purpose, the following scale variables are introduced: horizontal lengths x, $y \sim L$, depth $h \sim H$, velocities $\overline{u}$, $\overline{v} \sim U$, vorticity $\omega \sim \Omega$ and $U \sim \Omega L$. The turbulent diffusivity in shallow flow, $L/H \gg 1$, is
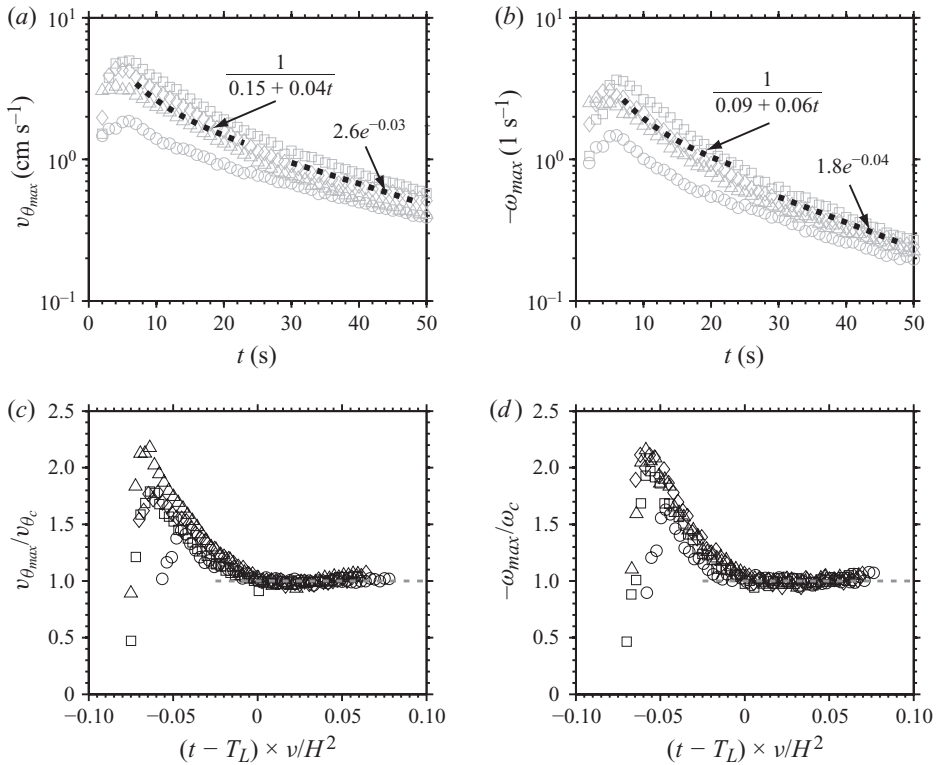
FIGURE 6. Time series of measured maximum azimuthal velocity (*a*) and vorticity (*b*) and non-dimensionalized maximum azimuthal velocity (*c*) and vorticity (*d*) with exponential decay model for various horizontal Reynolds numbers with the same shallowness ($S = 5$). $\circ$, $Re = 7850$; $\triangle$, $Re = 14\,000$; $\diamond$, $Re = 20\,000$; $\square$, $Re = 28\,000$. The dashed lines for early and late times, respectively, correspond to the first-order vortex model, (4.10) and (4.11), respectively.

governed by the bottom friction, $\nu_{eff} \sim \nu_{turb} = \beta u_* h$, in which $u_* = \sqrt{c_f/2}\sqrt{\overline{u}^2 + \overline{v}^2}$ is the shear velocity and β a constant (usually about 0.1) (Fischer *et al.* 1979). Thus, the order of magnitude for the turbulent diffusion term in (4.6) is $O(0.1\sqrt{c_f/2}(H/L)\Omega^2)$ and for the bottom friction term $O((c_f/2)(L/H)\Omega^2)$, respectively. With typical values of open channel flow friction coefficients, $c_f = 0.002 \sim 0.004$, for field and laboratory conditions (Uijttewaal & Booij 2000), the orders of magnitude for both terms are estimated as $O((0.003 \sim 0.005)(H/L)\Omega^2)$ and $O((0.001 \sim 0.002)(L/H)\Omega^2)$, respectively. This shows that the bottom friction term dominates over the turbulent diffusion term by a quadratic factor, $(L/H)^2$, and for $L/H \gg 1$, is practically solely responsible for the spin-down of isolated shallow turbulent vortex elements. On the other hand, the reverse argument holds for 'deep-water vortices': turbulent diffusion is the controlling factor, and bottom friction is unimportant.

4.2. *Decay of mean vortex properties*

The temporal decay of the maximum azimuthal velocity and vorticity of the vortex system for different initial angular velocity is shown in figure 6. Figures 6(*a*) and 6(*b*) show the maximum azimuthal velocity and vorticity from the ensemble-averaging described in §2.4 in dimensional form. It can be observed that the magnitudes increase until a certain time and then decrease gradually. The initial increase of
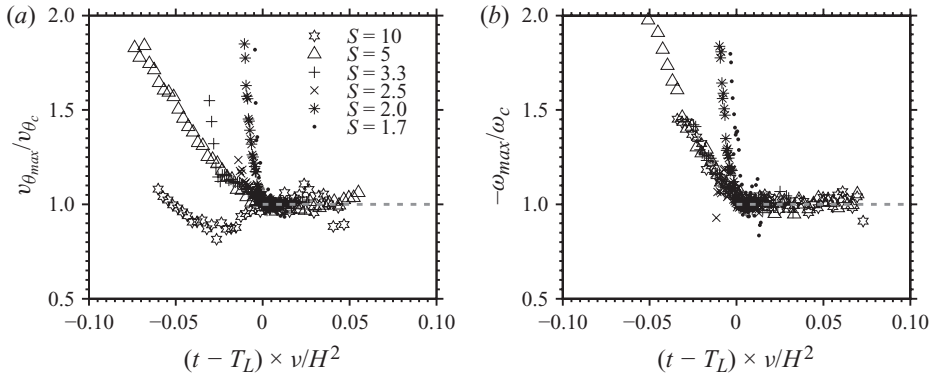
FIGURE 7. Time series of non-dimensionalized maximum azimuthal velocity (*a*) and vorticity (*b*) normalized with exponential decay model for various shallowness.

vorticity and azimuthal velocity magnitudes appears to be related to the transition from highly turbulent initial stage to quasi-two-dimensional flow. During this period, the maximum vorticity undergoes the initial oscillation until it reaches its peak value. This initial oscillation was observed and found to be related to the inertial surface waves with similar vortex generation method (Lodewijks 2008). Then, the whole vortex system starts decaying under the action of lateral entrainment of irrotational ambient fluid and bottom friction. As a result, the magnitudes of the azimuthal velocity and vorticity of the vortex decrease over time.

In two-dimensional axisymmetric flow, the decaying motion of a viscous flow can be expressed by $\omega = \exp(-\gamma^2 \nu t)$, where γ is a constant (see e.g. Batchelor 1967). To further study the decay properties of the vortex system, the exponential decay model was applied to the maximum vorticities as $\omega_{max}(t) = \omega_0' \exp(-\lambda t)$, where ω_0' is the initial maximum vorticity, and λ is the vorticity decay rate. Following Paireau, Tabeling & Legras (1997), it was assumed that the vortex system is dominated by rotational momentum initially and decays due to viscous dissipation after a certain time. When the maximum vorticity is normalized with the exponential decay model as the compensated maximum vorticity, $\omega_c = \omega_{max}(t)/\omega_0' \exp(-\lambda t)$, where ω_c' is obtained from the curve fit, then the compensated vorticity remains unity. This can also be applied to the azimuthal velocity, namely v_{θ_c} as the compensated azimuthal velocity. To test this assumption, we fitted the exponential decay curve backwards in time to obtain the vortex decay coefficient (λ) and transition time scale (T_L). Technically, the transition time scale is defined as the moment when the fitted curve deviates from the measured data significantly. This also represents the time for transition from turbulent to laminar flow condition. This vortex transition time can be comparable to the vertical viscous relaxation time estimated by $4H^2/9\pi^2\nu \sim 16\,\text{s}$ (Jüttner *et al.* 1997). Figures 6(*c*) and 6(*d*) and figure 7 show the compensated azimuthal velocity and vorticity for different Reynolds number and shallowness, respectively. In the plots, time coordinates are normalized with the transition time scale. In contrast to the same shallowness (figures 6*c* and 6*d*), the vortex decay is significantly different for various shallowness especially prior to transition time scale (figure 7). In table 2, the estimated transition time scale and exponential decay rate are presented. The physical interpretation of the transition time scale is discussed in detail in the following section.

Experiment number	T_{L_v} (s)	T_{L_ω} (s)	$\lambda_v \times 10^{-2}$ (1/s)	$\lambda_\omega \times 10^{-2}$ (1/s)
II	27.1	25.1	3.3	3.7
III	28.8	25.9	3.0	4.0
IV	28.9	27.0	3.6	4.5
V	27.7	24.1	4.0	5.3
VI	24.2	20.0	2.0	3.0
VII	28.4	24.8	1.6	2.4
VIII	18.1	21.6	1.4	1.2
IX	30.9	30.3	4.9	5.2

TABLE 2. Summary of the turbulent–laminar transition time scale (T_L) and the estimated exponential decay rate (λ). Subscripts v and ω represent the estimated values based on velocity and vorticity, respectively.

4.3. *Vortex decay model: first-order model*

A simple vortex model is presented here in order to explain the dominant first-order decay properties of the observed slowly growing system. Assuming at any instant of time a vortex of constant radius R that is subject to bottom friction, the force balance for a rotating fluid element at a distance, r, from the vortex centre is given by

$$\frac{d}{dt}(rVH) = -\frac{r\tau_b}{\rho}, \tag{4.7}$$

where V is azimuthal velocity at radial distance R, τ_b is bottom shear stress, H is water depth and ρ is water density. The bottom shear stress has different forms for turbulent and laminar conditions based on the Reynolds number. For the turbulent case, the bottom friction is given by

$$\frac{\tau_b}{\rho} = \frac{c_f}{2}V^2, \tag{4.8}$$

where c_f is the quadratic law friction coefficient. For the laminar case, and assuming a Poiseuille velocity profile in the vertical direction, the bottom friction can be expressed as

$$\frac{\tau_b}{\rho} = 3v\frac{V}{H}. \tag{4.9}$$

Integration of (4.7) with the shear stress non-dimensionalization leads to

$$V = \frac{1}{\dfrac{1}{V_0} + \dfrac{c_f}{2H}t} \tag{4.10}$$

for turbulent conditions, and to

$$V = V_0 \exp\left(-\frac{3v}{H^2}t\right) \tag{4.11}$$

for laminar conditions, respectively.

The established vortex decay models are compared in figure 6 with the experimental data as plotted with dotted lines. To demonstrate the goodness of the curve fit, we calculated the correlation coefficients as 0.98 for a turbulent region and 0.91 for a laminar region with the suggested functional relationships in the figure 6. These values represent that the curve fits reveal the underlying physics well. Figure 6(a), which
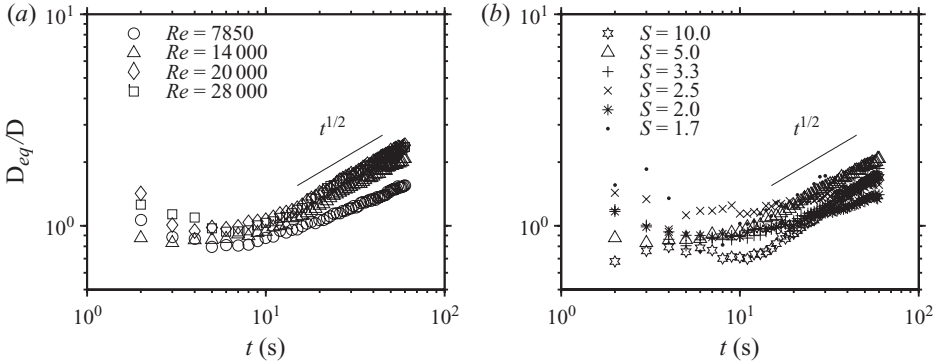
FIGURE 8. Estimated equivalent diameter of the vortex for different Reynolds numbers
(*a*) and shallowness (*b*).

is a semi-logarithmic representation of the maximum azimuthal velocity over time, demonstrates that the initial phase of the experiments for the first 10 to 25 s follows the turbulent spin-down result, $V \sim t^{-1}$ (see (4.10)). On the other hand, laminar spin-down, $V \sim e^{-t}$ (see (4.11)), controls the final phase of the vortex behaviour, after an initial period of about 30 s. In figure 6(*b*), the maximum vorticity also decays in the same manner with the azimuthal velocity. This is due to the fact that the maximum azimuthal velocity can be expressed by multiplying the maximum vorticity with the vortex radius.

A simple model for the vortex growth is given by

$$\sigma_r = \sqrt{2Et}, \tag{4.12}$$

where σ_r is the vortex radius (standard deviation of Gaussian distribution) and E is the diffusivity and for turbulent condition is given by

$$E \approx \nu_{turb} \approx u_* H \approx \sqrt{\frac{c_f}{2}} R_0 \Omega_0 H, \tag{4.13}$$

in which $u_* = \sqrt{(c_f/2)} V_0$ is the shear velocity, given by the initial value of the azimuthal velocity $V_0 = R_0 \Omega_0$. When comparing to the experimental data $\sigma_r(t)$ is taken as one half of the equivalent vortex diameter given by

$$D_{eq}(t) = \sqrt{4A_{vortex}/\pi}, \tag{4.14}$$

in which A_{vortex} is the area obtained from the vorticity contours. Figure 8 shows that the vortex growth exhibits a square root of time-dependence, $\sigma_r \sim t^{1/2}$ as given by (4.12). The low-Reynolds-number case ($Re = 7850$) in figure 8(*a*) is the exception to this square-root-dependence.

From the estimated equivalent vortex diameter and the measured maximum vorticity, we can define a local depth-based vortex Reynolds number as

$$Re_H(t) = \frac{\omega_{max}(t)\sigma_r(t)H}{\nu} \tag{4.15}$$

in order to characterize the turbulent–laminar transition state of the system. A critical value of Re_H can be taken as $Re_{H_{crit}} = 500$ as for open channel (Poiseuille) flow. The data comparison in figure 9 shows clearly that the transition from a turbulent to a laminar vortex state takes place typically at about $t = 15$–20 s for the conditions of our experiments.
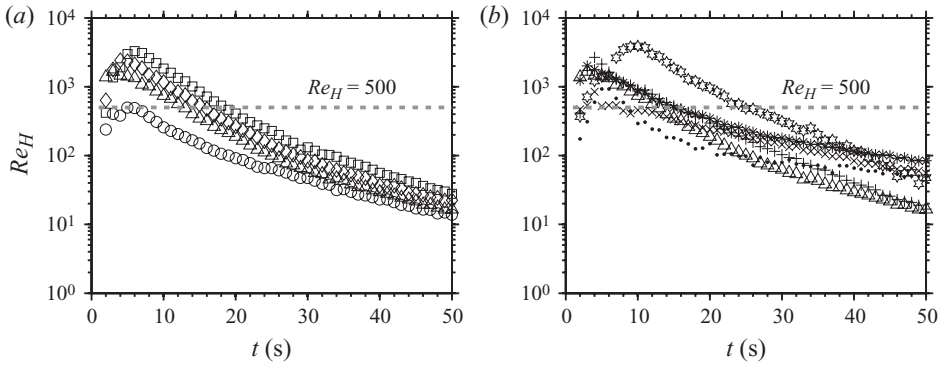
FIGURE 9. Transition of vortex Reynolds number for different Reynolds numbers (*a*) and shallowness (*b*). Symbols as in figure 8.
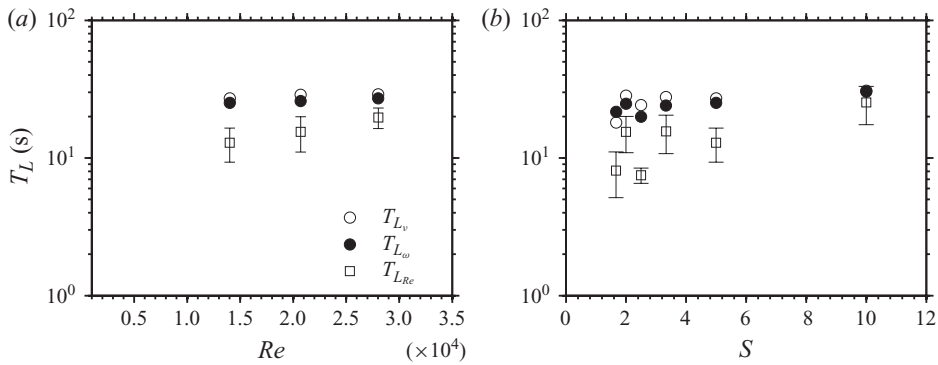

FIGURE 10. Comparison of the three different estimates for a turbulent–laminar transition time scale (T_L) for different Reynolds numbers (*a*) and shallowness (*b*). T_{L_v} and T_{L_ω} are defined in table 2. $T_{L_{Re}}$ is obtained from figure 9.

From the plots, another time scale for transition from turbulent to laminar condition can be obtained by measuring the time when the vortex Reynolds number goes below the critical number. We have plotted these transition time scales in figure 10 together with the transition time scales listed in table 2. The transition time scales obtained from the different methods show similar trends. The error bars in figure 10 were estimated from the standard deviation of the measured equivalent vortex diameter and maximum vorticity. In general, the transition time scale T_L appears to increase with increasing initial vortex Reynolds number Re and with increasing shallowness S. This means that vortices with stronger initial momentum remain in a turbulent state for a longer time. Furthermore, stronger shallowness limits the radial momentum transfer through three-dimensional horizontal diffusion and thus the spin-down to laminar conditions becomes delayed in comparison to deeper cases.

4.4. *Expansion of vortex decay model: second-order model*

In this section, the previous vortex decay model is extended by including the vortex expansion, which means that the vortex radius, R, is a function of time. Using the local moment of momentum method for pure azimuthal flows ($v_r = 0$) (Streeter & Wylie 1985), the angular momentum in the small fraction of a vortex patch with a thickness of dr and the distance of r from the vortex centre is balanced with the

bottom friction as

$$\frac{d}{dt}(r(2\pi r H \, dr)v_\theta) = -r\left(2\pi r \, dr \frac{\tau_b}{\rho}\right), \tag{4.16}$$

where H is the water depth, v_θ is the azimuthal velocity as a function of radial distance and τ_b is the bottom friction. If we integrate the above angular momentum balance over the whole vortex radius (R), we obtain

$$\int_0^R \frac{d}{dt}(r^2 v_\theta H) \, dr = -\int_0^R r^2 \frac{\tau_b}{\rho} \, dr. \tag{4.17}$$

Keeping in mind that the vortex radius is time-dependent, we can integrate the above equation using Leibnitz integration rule as follows:

$$\frac{d}{dt}\int_0^R (r^2 v_\theta H) \, dr - R^2 V H \frac{dR}{dt} = -\int_0^R r^2 \frac{\tau_b}{\rho} \, dr, \tag{4.18}$$

where V is the azimuthal velocity at radial distance R. We substitute the azimuthal velocity (v_θ) in the above equation with α-profile for the case of $\alpha = 2$ given by

$$v_\theta(r) = \frac{1}{2}\omega_0 r \, \exp\left(-\left(\frac{r}{R}\right)^2\right), \tag{4.19}$$

$$\omega(r) = \omega_0 \left(1 - \left(\frac{r}{R}\right)^2\right)\exp\left(-\left(\frac{r}{R}\right)^2\right), \tag{4.20}$$

in which ω_0 is the maximum vorticity, R is the radial distance, where the vorticity becomes null in this case (van Heijst & Clercx 2009). The bottom shear stress has different forms for turbulent and laminar conditions based on the Reynolds number as indicated in (4.8) and (4.9), respectively. On the other hand, the vortex radius can be estimated by introducing a simple model for the growth of the vortex as

$$\frac{dR^2}{dt} = E, \tag{4.21}$$

where E is the diffusivity, which can be the water viscosity (ν) for the laminar case and the turbulent diffusivity given by (4.13) for the turbulent case.

   After integrating (4.18) and substituting the azimuthal velocity (4.19), the governing equations for the laminar case are given by

$$\frac{d\omega_0}{dt} = \left[-\frac{1}{1 - 2/e}\left(4\left(1 - \frac{5}{2e}\right)\frac{\nu}{R^2} + 3\frac{\nu}{H^2}\right)\right]\omega_0, \tag{4.22}$$

$$\frac{dR}{dt} = \frac{\nu}{R}, \tag{4.23}$$

where e is the exponential. For the laminar case, the governing equations for the vortex decay can be solved by simple integration of (4.22) and (4.23). The value inside the square bracket on the right-hand side of (4.22) is comparable to the vortex decay rates (λ_v and λ_ω) from the previous section. For example, the vortex decay rate for the experiment II condition is estimated as 0.033 s^{-1} (table 2) and the value in the bracket is 0.032 s^{-1}.
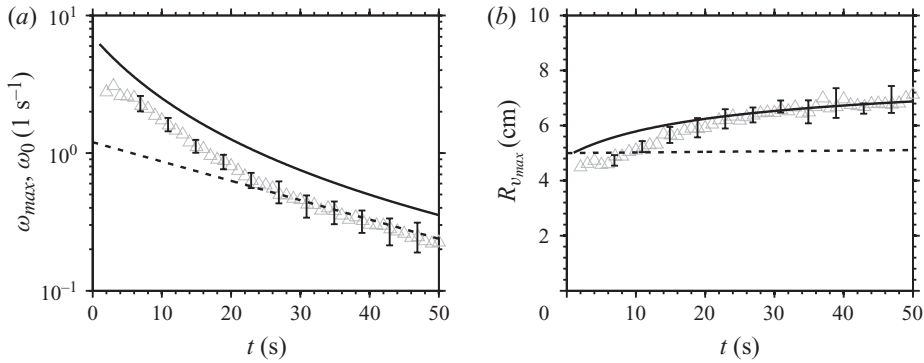
FIGURE 11. Comparison of the second-order vortex decay model and experimental results for maximum vorticity (*a*) and radial distance of peak velocity (*b*): △, measured results (experiment II). The solid and dotted lines are for the turbulent and laminar cases, respectively. Error bars represent the standard deviation in ensemble-averaging.

For the turbulent case using (4.13), the governing equations are given by

$$\frac{\mathrm{d}\omega_0}{\mathrm{d}t} = \left[-\frac{1}{\mathrm{e}-2} \left((2\mathrm{e}-5)\beta \sqrt{\frac{c_f}{2}} \frac{H}{R} + \frac{2\mathrm{e}}{5} c_f \frac{R}{H} \right) \right] \omega_0{}^2, \qquad (4.24)$$

$$\frac{\mathrm{d}R}{\mathrm{d}t} = \beta \sqrt{\frac{c_f}{2}} \omega_0 H. \qquad (4.25)$$

The results of the numerical integration of (4.22)–(4.25) are plotted in figure 11. The initial conditions for the numerical integration are taken from the experiment II case. The results for the laminar case are adjusted to match the measured maximum vorticity for the data after 25 s, where the laminar decay prevails (figure 11*a*). The slope of the numerical results for the laminar case appears to be reasonable within the standard deviation, though the radial distance of the peak velocity is much smaller than measured (figure 11*b*). For the turbulent case, the constant β has been calibrated with the measured radial distance of maximum azimuthal velocity, $R_{v_{max}}$, as shown in figure 11(*b*). Then, by taking the vortex radius into consideration, the maximum vorticities are obtained from the numerical integration with the fourth-order Runge–Kutta methods. The numerical integration results show a slight overestimation from the measured data. This seems to be related to the overestimation of the vortex radius, since the central vortex in the experiments undergoes significant deformations from circular to ellipsoidal shapes, as shown in figures 4 and 5.

5. Azimuthally averaged flow properties
5.1. *Mean flow profiles*

The azimuthally averaged flow properties of the vortex system evolving from the initial instability phase to its final tripolar form has been studied by means of the ensemble-averaging procedure. The velocity and vorticity profiles as a function of radial distance are plotted in figures 12 and 13. Figure 12 depicts the profiles for different Reynolds numbers at the initial stage ($t = 3.7$ s) for the same cylinder diameter ($D = 10$ cm) and water depth ($H = 2$ cm). In the plots, the radial distance is normalized with $R_{v_{max}}$, where the maximum azimuthal velocity is observed. The magnitudes of velocity and vorticity were also normalized with their maximum
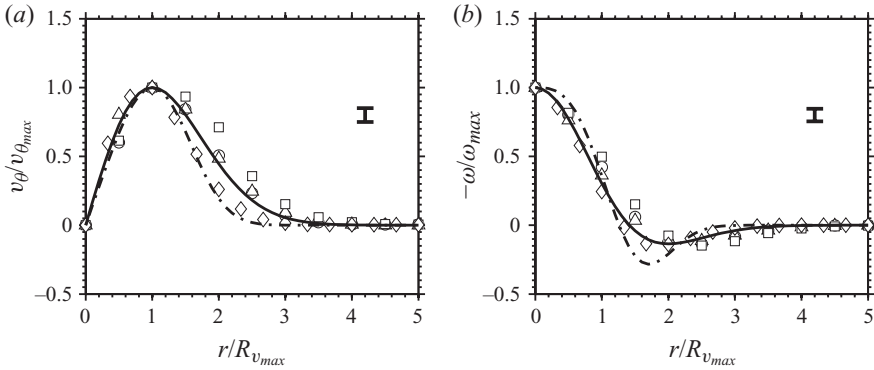
FIGURE 12. The non-dimensionalized profiles for measured azimuthal velocity (a) and vorticity (b) for the same shallowness ($S = 5$) at the initial stage $t = 3.7$ s. $\bigcirc$, $Re = 7850$; $\triangle$, $Re = 14\,000$; $\diamond$, $Re = 20\,000$; $\square$, $Re = 28\,000$. Solid line, $\alpha = 2$ (Gaussian vortex); dash-dotted line, $\alpha = 3$. Error bars represent the uncertainties of the measurements.
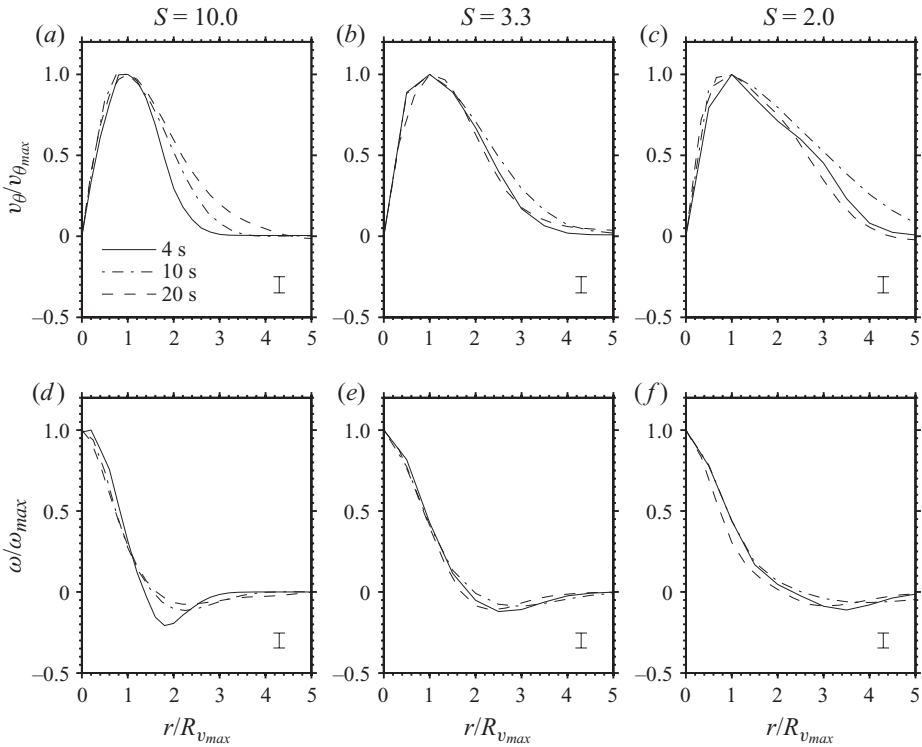

FIGURE 13. The non-dimensionalized profiles for measured azimuthal velocity (a–c) and vorticity (d–f) for different shallowness with the same Reynolds number ($Re = 14\,000$) and for different time steps. Error bars represent the uncertainties of the measurements.

values. The measured profiles are compared with proposed α-profile as in (4.19) and (4.20). This family of profiles has been used to study the stability of isolated circular vortices by adding small perturbations (Carton *et al.* 1989; Orlandi & van Heijst 1992; Carnevale & Kloosterziel 1994; Flór & van Heijst 1996). It has been

found in their studies that the profile becomes unstable for $\alpha > 1.85$ so that the instability behaviour depends on the shape of the initial vorticity distribution. For comparison, the Gaussian vortex ($\alpha = 2$) and steeper profile ($\alpha = 3$) (Carnevale & Kloosterziel 1994) have been plotted. The least-squares fit of (4.19) and (4.20) to the measured profile data yields $\alpha = 1.8 \sim 3.4$. This means that the individually generated monopolar vortex is strongly unstable and transforms into multipolar vortices. It is noteworthy that the steepness of the profile increases with Reynolds number. This means that a shallow vortex with higher Reynolds number will be more sensitive to small perturbations than those with small Reynolds number.

Figure 13 shows the effects of different shallowness: figure 13(*a–c*) shows the velocity profiles for different shallowness over increasing time (4, 10, 20 s); figure 13(*d–f*) represents the vorticity profile for the same conditions. For the strong shallowness case (figures 13*a* and 13*d*), the initial profiles show a very steep slope and become quickly flatter with increasing time. However, changes in profile are small for the weaker shallowness case (figures 13*c* and 13*f*). This contradicts a previous study on the radial velocity/vorticity profiles (Satijn *et al.* 2001), where the secondary circulation increases deformation of the radial profile with water depth. As shown in figure 5(*p*), however, the outside positive vortex patches do not aggregate together to form a large-scale structure but rather diffuse gradually in the deep-water case. When these patches are azimuthally averaged, the annular vorticity patches are smoothed out leading to gradual profile transition. In addition, as claimed by Lin *et al.* (2003), the shallowness accelerates the vorticity decay so that it is reasonable to see rapid adjustment in the profile in the strong shallowness case.

5.2. *Turbulence properties: turbulence intensity and Reynolds stress*

As described in the previous section, the initial stage of the shallow vortex flow is dominated by turbulence. To learn more about the turbulent properties generated by the single-vortex generation, the turbulent intensity and turbulent momentum flux are computed from the measured velocity fields.

The turbulence intensities plotted in figure 14 are defined as the root-mean-square (r.m.s.) values of velocity fluctuations, which are obtained from $v'_r(t) = v_r - \langle v_r \rangle$ and $v'_\theta(t) = v_\theta - \langle v_\theta \rangle$, respectively. Here, $\langle v_r \rangle$ and $\langle v_\theta \rangle$ are the azimuthally ensemble-averaged velocity components for radial and azimuthal directions respectively, as defined in §2.4. For small Reynolds number (figure 14*a*) and weak shallowness (figure 14*d*), the turbulent intensity profiles tend to decay while maintaining the shape of its profile in the radial direction. At the same time, the location of maximum turbulence intensity appears to remain near the vortex centre over time. On the contrary, the location of maximum turbulence intensity for large-Reynolds-number (figure 14*b*) and strong-shallowness (figure 14*c*) cases are moving outwards in the radial direction with increasing time. It is also interesting to observe a hump outside the central vortex. This hump appears to be related to the satellite vortex formation for the given experimental conditions.

With the simultaneous measurement of radial and azimuthal velocity components, one can obtain the Reynolds stresses as shown in figure 15. These stresses are responsible for transporting energy from the mean flow to the fluctuating turbulent flow (Dolzhanskii, Krymov & Manin 1992). A study of these characteristics is important for understanding the mechanism of turbulent energy transfer. For the strong shallowness case (figure 15*a*), the radius of the maximum azimuthal velocity consistently is overlapped with the inflection points of the Reynolds stress profile. However, for the weaker shallowness case (figure 15*b*), it is difficult to observe
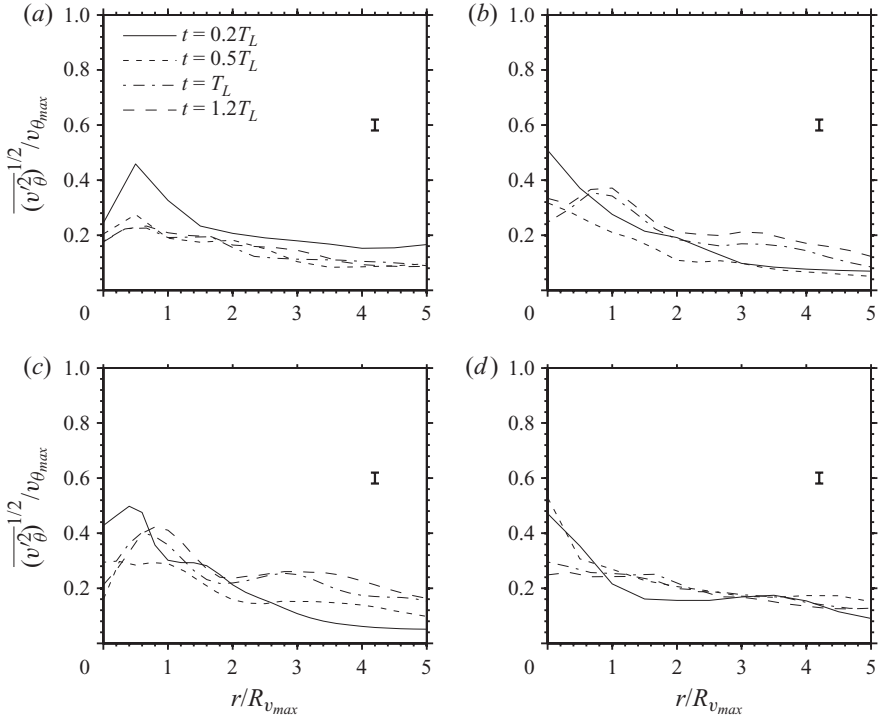
FIGURE 14. Turbulent intensity profiles for different vortex Reynolds numbers of 7850 (a) and 14 000 (b) with the same shallowness ($S = 5$) and for different shallowness of 10(c) and 2(d) for the same initial angular velocity ($\Omega_0 = 6.28\,\mathrm{s}^{-1}$) at different times. Note that transition time scale T_L is based on the azimuthal velocity. Error bars represent the uncertainties of the measurements.
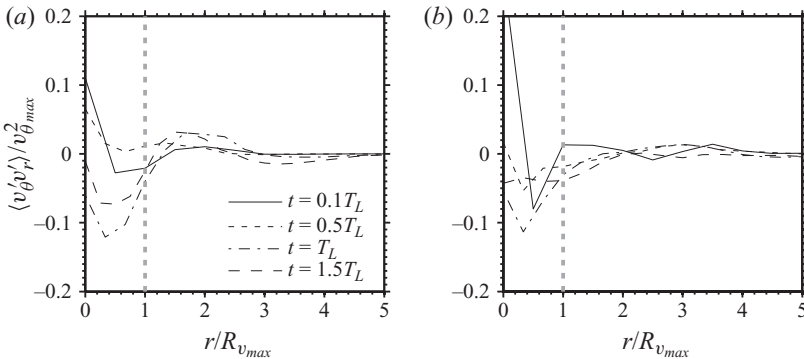

FIGURE 15. Reynolds stress distribution as a function of radial distance for the cases of $Re = 14\,000$ with $S = 5$ (a) and $Re = 14\,000$ at $S = 2$ (b).

any distinguished inflection points from the measured Reynolds stress profile. Furthermore, the Reynolds stresses tend to vanish quickly with increasing radial distance. Thus, the shallow vortex system maintains itself relatively longer than the corresponding deep-water case.

5.3. *Instability of the shallow vortex*

In this section, the causes of the formation of large-scale coherent structures in the shallow vortex flow are analysed. As observed, the vortex system for strong shallowness and high *Re* converges to a tripolar system. In order to analyse the background physics on this tripole formation, we assume that the complex vortex system can be approximated by the sum of harmonic functions with different wavenumbers k (Kloosterziel & Carnevale 1999). As we observe in dye visualization tests (not shown here), there is strong vertical and horizontal mixing around the central vortex when the cylinder is lifted vertically, and it can be postulated that the small perturbation from this initial turbulent stage leads to the development of an azimuthal wavenumber 2 mode. Previous studies indicate that the wavenumber 2 mode is the fastest-growing perturbation mode for a steep vorticity profile (Carnevale & Kloosterziel 1994).

To quantitatively investigate this assumption, the mean instability amplitude of an instantaneous vorticity field is evaluated by averaging the mode amplitudes of the ensemble-averaged vorticity data sets. Following Kloosterziel & Carnevale (1999), we assume that the vorticity field can be expressed as $\sum_{k=0}^{\infty} \omega_k$, where

$$\omega_k = f_k(r;t) \, \mathrm{Re}\left(e^{ik\theta+i\phi_k(r;t)}\right), \qquad (5.1)$$

in which $\mathrm{Re}(\cdot)$ denotes the real part and $\phi_k = 0$ for $k = 0$. The $f_k(r;t)$ and the phase factors can be determined numerically using $C_k = f_k \cos(\phi_k)$, $S_k = f_k \sin(\phi_k)$ with

$$\{C_k(r;k), S_k(r;k)\} = \frac{1}{\pi} \int_0^{2\pi} \omega(r,\theta;t)\{\cos(k\theta), \sin(k\theta)\} \, \mathrm{d}\theta. \qquad (5.2)$$

This gives a decomposition of the vorticity distribution in the azimuthal direction. For any given time, the amplitude of the azimuthal vorticity for each wavenumber can be obtained as

$$A_k(t) = \left(\int_0^{2\pi} \int_0^{\infty} \omega_k^2(r,\theta;t) r \, \mathrm{d}r \, \mathrm{d}\theta \right)^{1/2}. \qquad (5.3)$$

Figure 16 shows the temporal evolution of the perturbation spectra for the same Reynolds number and different shallowness. Note that the amplitudes of each wavenumber were normalized with A_0, which is the wave amplitude of the mean flow. For the shallow-water case (figure 16(*a*)–(*d*)), it is apparent that the most unstable mode wavenumber $k = 2$ grows exponentially. The amplitude of the perturbation wavenumber $k = 4$ is also growing, but remains smaller than A_2 by around 30 %. For the deep-water case (figure 16(*e*)–(*h*)), the increasing rate of A_2 is much slower, which means that the tripole formation is much less pronounced than for a shallow water vortex.

In figure 17, the amplitude growth rates of the perturbation wavenumber 2 are plotted for different Reynolds numbers and shallowness. To evaluate this growth rate, we selected the exponentially growing regime of the wave amplitude. It can be observed that the perturbation wave amplitude grows in an exponential manner until it saturates (Carton & Legras 1994; Kloosterziel & Carnevale 1999). The growth rates were determined by fitting on exponential curve, $\exp(\sigma t)$, to the A_2 values from figure 16. For comparison, we also plotted the growth rates estimated from figure 1(*b*) in Kloosterziel & Carnevale (1999) using the coefficient α from the measured initial velocity profile. For the α values less than 2, which is outside the data they provided, we extrapolated from their data points. It can be observed that both increasing
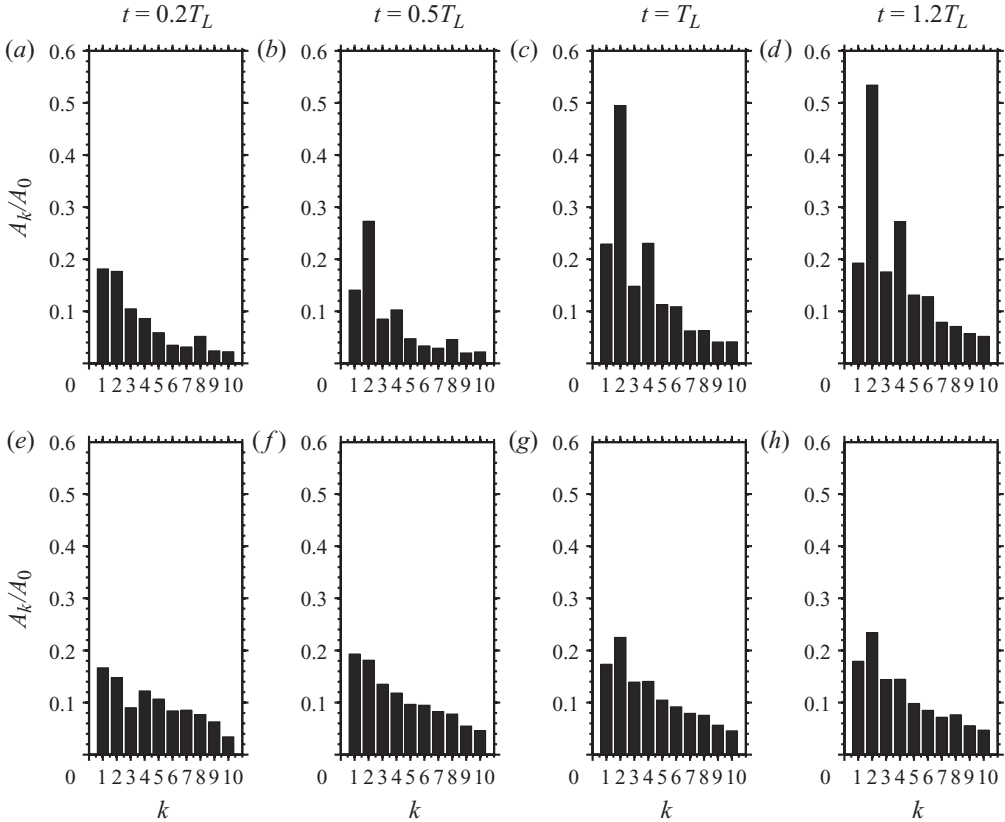
FIGURE 16. Perturbation spectra for $Re = 14\,000$ for the shallow case $S = 5$ (a–d), and for the deep case $S = 2$ (e–h) at different times.
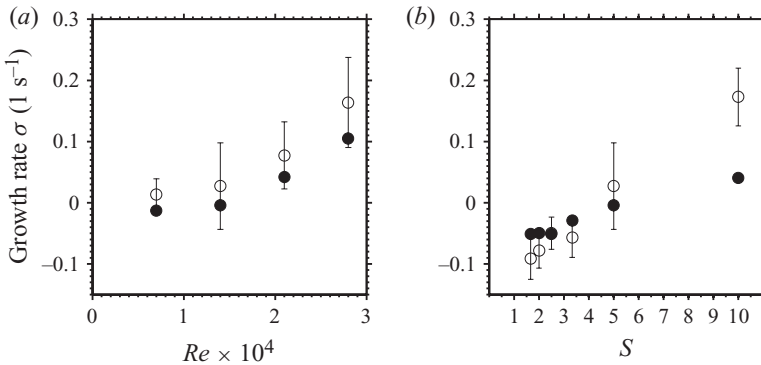

FIGURE 17. The growth rates for azimuthal perturbation wavemode number 2 as a function of Reynolds number (a) and shallowness (b). Empty circles are the measured data and filled circles the estimated growth rate from Kloosterziel & Carnevale (1999) using α based on the initial radial velocity profile. Error bars represent standard deviations from different data sets.

shallowness and increasing Reynolds number contribute to the development of an azimuthal wavenumber $k = 2$ regime. As pointed out in Satijn et al. (2001), the evolution of a shallow vortex depends not only on the shallowness but also on

the dynamical effect represented by the Reynolds number, which results in a strong secondary vertical flow.

6. Conclusions

The evolution and decay of shallow-water vortices were investigated with laboratory experiments without background rotation. Emphasis was placed on the effects of the initial vortex Reynolds number and the shallowness, the ratio of the horizontal length scale of a vortex to the water depth. A single vortex was generated by spinning a water mass using a bottomless cylinder with internal sectors. From the estimated vorticity fields, it was found that strong shallowness and high Reynolds number contribute to the formation of large-scale coherent structures in the form of a tripolar vortex. The following major results of the present study can be stated as conclusions.

(i) The investigation on the measured vorticity maps clearly exhibited that there is Reynolds-invariant behaviour of the shallow water vortices. Qualitative and quantitative measurements have shown that the generated single vortices converge to a tripolar system for high Reynolds numbers ($Re \geqslant 14\,000$) and strong shallowness ($S \geqslant 4$). This property of the shallow vortex leads to formation of a tripolar vortex for strong shallowness conditions. For weak shallowness conditions, it appears that the horizontal turbulent diffusion of momentum inhibits the formation of large-scale coherent structures.

(ii) It was shown that the shallow-water vortices with high initial Reynolds numbers experience the transition from turbulent to laminar regimes in their decay process. Based on the angular momentum balance between rotational momentum and bottom friction, the proposed first-order vortex decay model predicts that a shallow-water vortex decays as t^{-1} for the turbulent case and as e^{-t} for the laminar case. The experimental data are in good agreement with this vortex decay model, in which horizontal diffusion and bottom friction are principal causes of the vortex decay as we found in the scale analysis. The estimated transition time scale from turbulent to laminar regime has been found to increase with increasing initial vortex Reynolds number and with increasing shallowness. This can be attributed to the fact that vortices with stronger initial momentum remain in a turbulent state for a longer time. Furthermore, the vortex expansion effect has been included in the second-order model, where the overestimation of vortex radius results in a slightly higher magnitude of vorticity than the measured one.

(iii) The ensemble statistics obtained by averaging over the azimuthal direction of the measured velocity/vorticity data elucidated effects of the vortex instabilities and of turbulent energy transfer on the formation of large-scale coherent flow structure. The estimated turbulence intensity and Reynolds stress showed that turbulent energy is transferred to the satellite vortices under strong shallowness and high-Reynolds-number conditions.

(iv) Normal mode analysis of the generated vortex systems demonstrated that the shallowness and the Reynolds number are the important factors in forming two-dimensional large-scale coherent structures. As previous theoretical and numerical studies have found, the perturbation wavenumber 2 mode is the fastest-growing instability in shallow-water conditions. This analysis clearly shows that increasing the water depth results in a suppression of the quasi-two-dimensional flow features.

Further experiments are in progress in order to investigate the detailed vertical structure of shallow-water vortices. Even at small water depths, three-dimensional effects play an important role in the vortex dynamics as shown by Akkermans *et al.*

(2008). Research is required to understand the effects of three-dimensional instabilities on the large-scale dynamics of predominantly two-dimensional flow.

REFERENCES

AKKERMANS, R. A. D., CIESLIK, A. R., KAMP, L. P. J., TRIELING, R. R., CLERCX, H. J. H. & VAN HEIJST, G. J. F. 2008 The three-dimensional structure of an electromagnetically generated dipolar vortex in a shallow fluid layer. *Phys. Fluids* **20** (11), 116601–116615.

BATCHELOR, G. K. 1967 *An Introduction to Fluid Dynamics*. Cambridge University Press.

BECKERS, M. & VAN HEIJST, G. J. F. 1998 The observation of a triangular vortex in a rotating fluid. *Fluid Dyn. Res.* **22** (5), 265–279.

CARMER, C. F. v., RUMMEL, A. C. & JIRKA, G. H. 2004 Influx of secondary motion in large-scale coherent vortical structures on the mass transport in a shallow turbulent wake flow. In *Shallow Flows*. Balkema.

CARNEVALE, G. F. & KLOOSTERZIEL, R. C. 1994 Emergence and evolution of triangular vortices. *J. Fluid Mech.* **259**, 305–331.

CARTON, X. J. 2001 Hydrodynamical modeling of oceanic vortices. *Surv. Geophys.* **22** (3), 179–263.

CARTON, X. J., FLIERL, G. R. & POLVANI, L. M. 1989 The generation of tripoles from unstable axisymmetric isolated vortex structures. *Europhys. Lett.* **9** (4), 339–344.

CARTON, X. & LEGRAS, B. 1994 The life-cycle of tripoles in two-dimensional incompressible flows. *J. Fluid Mech.* **267**, 53–82.

CENEDESE, C., ADDUCE, C. & FRATANTONI, D. M. 2005 Laboratory experiments on mesoscale vortices interacting with two islands. *J. Geophys. Res.* **110**, C09023.

CHEN, D. & JIRKA, G. H. 1995 Experimental study of plane turbulent wakes in a shallow water layer. *Fluid Dyn. Res.* **16** (1), 11–41.

CLERCX, H. J. H., VAN HEIJST, G. J. F. & ZOETEWEIJ, M. L. 2003 Quasi-two-dimensional turbulence in shallow fluid layers: the role of bottom friction and fluid layer depth. *Phys. Rev.* E **67** (6), 066303.

CREUTIN, J. D., MUSTE, M., BRADLEY, A. A., KIM, S. C. & KRUGER, A. 2003 River gauging using PIV techniques: a proof of concept experiment on the Iowa river. *J. Hydrol.* **277** (3–4), 182–194.

DOLZHANSKII, F. V., KRYMOV, V. A. & MANIN, D. YU. 1992 An advanced experimental investigation of quasi-two-dimensional shear flow. *J. Fluid Mech.* **241**, 705–722.

FISCHER, H. B., LIST, E. G., KOH, R. C. Y., IMBERGER, J. & BROOKS, N. H. 1979 *Mixing in Inland and Coastal Waters*. Academic.

FLIERL, G. R. 1988 On the instability of geostrophic vortices. *J. Fluid Mech.* **197**, 349–388.

FLÓR, J. B. & VAN HEIJST, G. J. F. 1996 Stable and unstable monopolar vortices in a stratified fluid. *J. Fluid Mech.* **311**, 257–287.

FUJITA, I., MUSTE, M. & KRUGER, A. 1998 Large-scale particle image velocimetry for flow analysis in hydraulic engineering applications. *J. Hydraul. Res.* **36** (3), 397–414.

VAN HEIJST, G. J. F. & CLERCX, H. J. H. 2009 Laboratory modeling of geophysical vortices. *Annu. Rev. Fluid Mech.* **41** (1), 143–164.

VAN HEIJST, G. J. F. & FLÓR, J. B. 1989 Dipole formation and collisions in a stratified fluid. *Nature* **340** (20), 212–215.

VAN HEIJST, G. J. F. & KLOOSTERZIEL, R. C. 1991 Laboratory experiments on the tripolar vortex in a rotating fluid. *J. Fluid Mech.* **225**, 301–331.

JIRKA, G. H. 2001 Large scale flow structures and mixing processes in shallow flows. *J. Hydraul. Res.* **39** (6), 567–573.

JIRKA, G. H. & SEOL, D.-G. 2010 Dynamics of isolated vortices in shallow flows. *J. Hydro-Environ. Res.* **4** (2), 65–73.

JIRKA, G. H. & UIJTTEWAAL, W. S. J. 2004 *Shallow Flows*. Balkema.

JÜTTNER, B., MARTEAU, D., TABELING, P. & THESS, A. 1997 Numerical simulations of experiments on quasi-two-dimensional turbulence. *Phys. Rev. E* **55** (5), 5479–5488.

KLOOSTERZIEL, R. C. & CARNEVALE, G. F. 1999 On the evolution and saturation of instabilities of two-dimensional isolated circular vortices. *J. Fluid Mech.* **388**, 217–257.

KLOOSTERZIEL, R. C. & VAN HEIJST, G. J. F. 1991 An experimental study of unstable barotropic vortices in a rotating fluid. *J. Fluid Mech.* **223**, 1–24.

KLOOSTERZIEL, R. C. & VAN HEIJST, G. J. F. 1992 The evolution of stable barotropic vortices in a rotating free-surface fluid. *J. Fluid Mech.* **239**, 607–629.

LEGRAS, B., SANTANGELO, P. & BENZI, R. 1988 High-resolution numerical experiments for forced two-dimensional turbulence. *Europhys. Lett.* **5**, 37–42.

LIN, J.-C., OZGOREN, M. & ROCKWELL, D. 2003 Space–time development of the onset of a shallow-water vortex. *J. Fluid Mech.* **485**, 33–66.

LODEWIJKS, B. B. F. M. 2008 Experiments on barotropic vortex instabilities in a rotating fluid. *Tech. Rep.* R-1737-A. Eindhoven University of Technology.

MCWILLIAMS, J. C. 1984 The emergence of isolated coherent vortices in turbulent flow. *J. Fluid Mech.* **146**, 21–43.

MEINHART, C. D., WERELEY, S. T. & SANTIAGO, J. G. 2000 A PIV algorithm for estimating time-averaged velocity fields. *J. Fluids Engng* **122** (2), 285–289.

MESELHE, E. A., PEEVA, T. & MUSTE, M. 2004 Large scale particle image velocimetry for low velocity and shallow water flows. *J. Hydraul. Engng* **130** (9), 937–940.

NGUYEN DUC, J.-M. & SOMMERIA, J. 1988 Experimental characterization of steady two-dimensional vortex couples. *J. Fluid Mech.* **192**, 175–192.

NICOLAU DEL ROURE, F., SOCOLOFSKY, S. A. & CHANG, K.-A. 2009 Structure and evolution of tidal starting jet vortices at idealized barotropic inlets. *J. Geophys. Res.* **114**, C05024.

ORLANDI, P. & CARNEVALE, G. F. 1999 Evolution of isolated vortices in a rotating fluid of finite depth. *J. Fluid Mech.* **381**, 239–269.

ORLANDI, P. & VAN HEIJST, G. J. F. 1992 Numerical simulation of tripolar vortices in 2D flow. *Fluid Dyn. Res.* **9**, 179–206.

PAIREAU, O., TABELING, P. & LEGRAS, B. 1997 A vortex subjected to a shear: an experimental study. *J. Fluid Mech.* **351**, 1–16.

PARET, J., MARTEAU, D., PAIREAU, O. & TABELING, P. 1997 Are flows electromagnetically forced in thin stratified layers two dimensional? *Phys. Fluids* **9** (10), 3102.

PINGREE, R. D. & LE CANN, B. 1992 Three anticyclonic slope water oceanic eddies (SWODDIES) in the southern bay of Biscay in 1990. *Deep Sea Res.* I **39** (7–8), 1147–1175.

RAFFEL, M., WILLERT, C. & KOMPENHANS, J. 1998 *Particle Image Velocimetry: A Practical Guide*. Springer.

SATIJN, M. P., CENSE, A. W., VERZICCO, R., CLERCX, H. J. H. & VAN HEIJST, G. J. F. 2001 Three-dimensional structure and decay properties of vortices in shallow fluid layers. *Phys. Fluids* **13** (7), 1932–1945.

SOUS, D., BONNETON, N. & SOMMERIA, J. 2005 Transition from deep to shallow water layer: formation of vortex dipoles. *Eur. J. Mech.* B *Fluids* **24** (1), 19–32.

STREETER, V. L. & WYLIE, E. B. 1985 *Fluid Mechanics*, 8th edn. McGraw-Hill.

SUKHODOLOV, A., UIJTTEWAAL, W. S. J. & ENGELHARDT, C. 2002 On the correspondence between morphological and hydrodynamical patterns of groyne fields. *Earth Surf. Process. Landf.* **27** (3), 289–305.

TRIELING, R. R. & VAN HEIJST, G. J. F. 1998 Decay of monopolar vortices in a stratified fluid. *Fluid Dyn. Res.* **23** (1), 27–43.

UIJTTEWAAL, W. S. J. & BOOIJ, R. 2000 Effects of shallowness on the development of free-surface mixing layers. *Phys. Fluids* **12**, 392–402.

VOROPAYEV, S. I., MCEACHERN, G. B., BOYER, D. L. & FERNANDO, H. J. S. 1999 Experiment on the self-propagating quasi-monopolar vortex. *J. Phys. Oceanogr.* **29**, 2741–2751.

WELLS, M. G. & VAN HEIJST, G. J. F. 2003 A model of tidal flushing of an estuary by dipole formation. *Dyn. Atmos. Oceans* **37**, 223–244.

ZAVALA SANSÓN, L. & VAN HEIJST, G. J. F. 2002 Ekman effects in a rotating flow over bottom topography. *J. Fluid Mech.* **471**, 239–255.